Elastic bound modes in the continuum in architected beams

Adib Rahman and Raj Kumar Pal[*]

Department of Mechanical and Nuclear Engineering, Kansas State University, Manhattan, Kansas 66506, USA

We report the experimental observation of an elastic bound mode in the continuum (BIC) in a compact region of an architected beam. We consider a long slender beam with rigid masses attached at periodic intervals, with a compact segment bounded by four protruding side beams. The key idea is to seek a mode where the side beams move out of phase with the compact region, thereby nullifying the forces and moments outside this region and resulting in a bound mode. The structure is modeled with use of Euler-Bernoulli beam theory and the side beams are designed by our imposing equilibrium constraints required for a BIC. Multiple bound modes in the continuum are found in the compact region, and for each BIC, we find a one-parameter family of BIC-supporting side-beam designs. The predictions are verified by three-dimensional finite-element simulations, followed by their experimental observation by laser Doppler vibrometry in a macroscale structure. Our approach allows one to achieve bound modes in the continuum in an arbitrary-sized compact region of the architected beam. Our findings may open avenues for confining elastic wave energy in compact regions for applications in sensors and resonators.

I. INTRODUCTION

Bound modes in the continuum (BICs) are a unique class of localized modes with two key properties: their wave amplitude diminishes to zero outside a compact region and their frequency is in the continuous spectrum (passband) of bulk propagating modes [1]. In contrast, conventional bound modes reside within band gaps, and the localized modes encountered in the passband typically exhibit leakage, with the wave amplitude gradually decreasing from the center of the wave [2–4]. The concept of BICs originated in quantum mechanics, introduced in 1929 by von Neumann and Wigner [5], who used a complex artificial potential. It was regarded as a mathematical anomaly, as such complex potentials were not possible in real materials. BICs were subsequently predicted and observed in several classical wave systems [6,7]. Notably, in 1966, BICs were experimentally observed in acoustics through the "wake-shedding experiment" [8]. Today, BICs have become an active area of research across various scientific disciplines due to their leak-free energy-storage capacity with a very high quality factor (Q factor) [9]. Potential applications of BICs encompass lasing [10–12], sensing [13], filtering [14,15], supersonic surface acoustic devices [16,17], vibration absorption [18], and wave guiding [19–21].

Recent advancements in manufacturing techniques have opened up new possibilities for exploring BICs in complex structures, particularly in the domains of photonic

metamaterials. Two major types of BICs are symmetry-protected BICs and accidental BICs. Symmetry-protected BICs arise from the mismatch between the spatial symmetry of a localized mode and the symmetry of the propagating modes. Experimental observations of such symmetry-protected BICs have been reported in various systems, such as dielectric slabs with square arrays of cylinders [22], periodic chains of dielectric disks [23], and optical waveguides [24]. On the other hand, accidental BICs can be achieved through precise system-parameter tuning to cancel their coupling with bulk propagating waves. An example of this category is the Fabry-Perot bound mode in the continuum (BIC) [25,26], where the BIC is formed through the destructive interference of waves. In addition to these two types of BICs, recent research has explored quasi-BICs, which have high Q factors [27,28]. As true BIC-supporting structures are limited, quasi-BICs are emerging as an alternative.

In contrast to photonics, a major challenge in achieving elastic BICs is the simultaneous presence of transverse and longitudinal waves with distinct dispersion relations. BICs should not couple or hybridize with any propagating modes present in an elastic body. Haq and Shabanov [29] theoretically predicted Fabry-Perot BICs for an in-plane wave with scatterers, using distinct densities but the same Lamé constants for the background material and scatterers. Cao *et al.* [18,30] experimentally demonstrated wave confinement at the boundary of an elastic plate for transverse waves incident at a specific angle. Their design uses an array of resonators embedded at the plate boundary. Fan *et al.* [31] observed BICs in a non-Hermitian system by

---
[*]rkpal@ksu.edu

exploiting damping and boundary conditions. BICs have also been observed in multiphysics domains, including in chip-scale ring-shaped optomechanical microresonators [32], slab-on-substrate phononic crystals [33], and an elastic bar with an air-encapsulated cavity [34]. All these BICs require specific material properties, boundary conditions, geometric features, or properties such as damping and multiphysics interactions. For practical applications, it is desirable to have a general framework that can translate across material properties and generate BICs in arbitrary-sized compact regions.

This work builds on our prior work [21], where we predicted how a family of BICs can be achieved in an arbitrary compact region of a spring-mass system by exploiting symmetry constraints. Here we extend this concept to realize BICs in a compact region of an architected beam. In contrast to spring-mass chains, beams are continuous structures with multiple degrees of freedom at each point—namely, transverse displacements and rotations. These degrees of freedom impose additional conditions for BICs. Here we consider a periodic architected beam having an array of rigid masses. To achieve BICs in a compact region, four side beams are added, and the key idea is that they move out of phase with the periodic beam to nullify forces and moments at their joints. Compared with previous work, our concept provides a framework to confine an elastic wave at an arbitrary location in a beam structure. The frequency and length of the confined region can be independently varied by change of the size and location of the rigid masses. In addition, the concept translates across material properties and length scales.

The outline of this paper is as follows: Sec. II presents the design and modeling approach. The structure is modeled with use of one-dimensional (1D) Euler-Bernoulli beam theory. Section III represents the mode

shapes of BICs determined with use of 1D finite-element analysis and reports a one-parameter family of BIC-supporting side beam designs. In Sec. IV, three-dimensional (3D) finite-element simulations and laser Doppler vibrometry–based experimental measurements are presented that verify and validate the existence of a BIC in the architected structure. The simulations are done with use of the beam theory–based design as a starting point to finalize a structure that simplifies fabrication. Finally, the conclusions, along with various sources of error and possible future extensions, are presented in Sec. V.

II. PROPOSED CONCEPT AND MODELING APPROACH TO DESIGN THE COMPACT REGION

We first introduce the proposed architected beam and discuss the key idea of achieving BICs in a compact region by adding side beams. These side beams are designed by modeling the structure using a 1D Euler-Bernoulli beam theory. A description of this modeling approach is presented, followed by its numerical discretization procedure.

A. Architected beams with side segments and symmetry consideration

We consider a homogeneous beam with rigid masses attached at periodic intervals of distance l. An example is shown in the central beam in Fig. 1(a). We call this periodic architected beam the "main beam." Figure 1(b) displays a unit cell of the main beam with the key geometric variables labeled. It is a slender beam with rectangular cross section and has two identical rigid cylinders at its center, one at the top and one at the bottom. Note that rigid masses in the main beam allow independent control over the length of region in which a BIC is confined and its frequency.
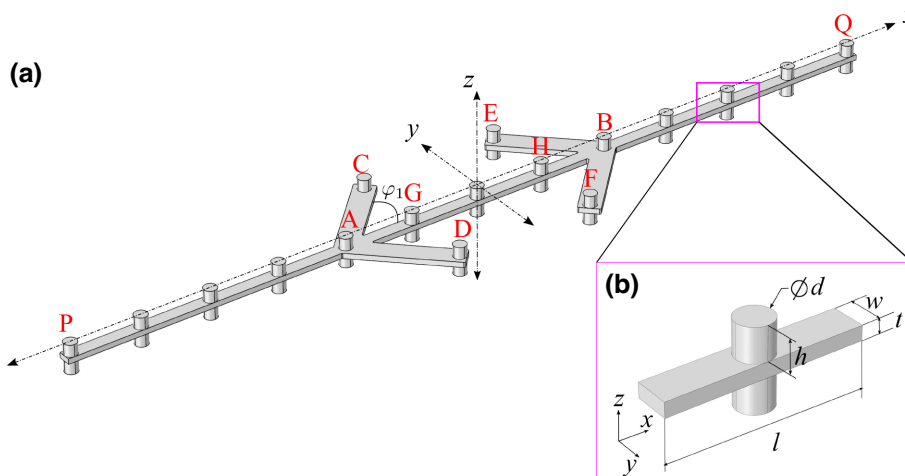
FIG. 1. (a) Proposed architected beam: rigid masses attached at periodic intervals along a homogeneous beam. Four side beams are added to get a BIC between the cross sections at A and B. (b) A unit cell of the periodic beam with the key geometric variables labeled.

Our objective is to achieve a BIC in an arbitrary compact region, for example, between the cross sections labeled "*A*" and "*B*" in Fig. 1(a). We model this architected structure using 1D beam theory, which assumes that the beam deforms such that each cross section remains rigid. Under this assumption, the degrees of freedom are the three translations and three rotations of each cross section along the beam's axis. We restrict our attention to long wavelengths, compared with the beam thickness, and low frequencies, i.e., in the first passband of the beam. The lower-frequency band has flexural modes with displacement along the *z* axis. For such modes, it suffices to consider two degrees of freedom at each cross section: transverse displacement *u* along the *z* axis and rotation θ about the *y* axis, with the latter accounting for bending. The presence of side beams couples the torsional (rotation about the *x* axis) and flexural modes near the compact region. However, as we discuss below, for BICs, the rotation about the *x* axis is canceled due to symmetry, and thus the number of relevant degrees of freedom at each point along the beam cross section is 2.

A BIC between cross sections *A* and *B* will be a mode confined in this region and with zero displacement and rotation at all points outside the region, i.e., in the segments *AP* and *BQ*. Our approach is to add side beams, as displayed in Fig. 1(a), that cancel the motion outside the compact region. We first present the conditions that ensure a bound mode in the compact region. We enforce zero displacement, rotation, net force, and moment at the boundaries of the compact region, i.e., at cross sections *A* and *B*. These conditions at cross section *A* may be written as

$$\sum F_{zA} = 0, \ \sum M_{xA} = \sum M_{yA} = 0, \ u_A = 0, \ \theta_A = 0. \tag{1}$$

Note that only the contributions from the compact region and the side beams are considered in the forces and moments in Eq. (1).

To see why the above-mentioned conditions imply that segment *AP* in Fig. 1(a) is at rest, we consider an initial-boundary-value problem on segment *AP* when Eq. (1) is satisfied. This segment has no external forces and its boundaries have zero displacement. The zero-displacement field ($\boldsymbol{u} = [u_x \ u_y \ u_z]^T = \boldsymbol{0}$) throughout segment *AP* is a valid solution since it satisfies the equilibrium conditions at each point as well as all the boundary conditions. Since the governing equations, namely, the Cauchy equations for elastodynamics, or the one-dimensional Euler-Bernoulli beam theory are linear, the solution ($\boldsymbol{u} = \boldsymbol{0}$) is unique. Thus, the conditions in Eq. (1) ensure zero displacement in segment *AP*, regardless of its size or the boundary type at cross section *P*. Conditions similar to Eq. (1) at cross section *B* ensure that segment *BQ* is at rest, thereby implying a BIC confined in segment *AB*, along with the side beams.

We now discuss how the side beams in Fig. 1(a) induce BICs. The key idea is to have a mode where the side beams move out of phase, i.e., in a direction opposite that of the main beam, thereby canceling the net force and moment at cross sections *A* and *B*. In addition, as we explained above, enforcing zero displacement and rotations at these cross sections results in the far field being at rest. Finally, we remark on the reason for having two side beams, one on either side, at cross sections *A* and *B*. A single side beam will induce torsional rotation about the main beam axis due to the moment component M_x. To cancel this moment, a second side beam is added. The two side beams on either side at cross section *A* thus move in phase with each other, but out of phase with the main beam. We show in Sec. III a family of side beams that can satisfy Eq. (1), i.e., cancel displacement, rotation, force, and moment at cross sections *A* and *B*.

We choose all the side beams to be identical and arrange them so that the center of the compact region between cross sections *A* and *B* has reflection symmetry about both the *x* axis and the *y* axis. Note that BICs do not require these symmetries, and they are chosen to simplify the side-beam design. Indeed, the only requirement to ensure zero displacement and rotation outside the compact region is that the conditions of Eq. (1) are satisfied at cross sections *A* and *B*. We remark here that the full design space of distinct side beams is sufficiently large, with multiparameter families of solutions that satisfy these conditions. Imposing the constraints arising for symmetry, we find that the problem of inducing BICs reduces to determining suitable side beams. As we are considering that the side beams' arrangement is reflection-symmetric about the *x* and *y* axes, determining one side beam's design will suffice to complete the beam structure that can support a BIC at a particular frequency.

We now discuss how these reflection symmetries and equilibrium conditions impose restrictions on the resulting bound mode shapes in the compact region. Each symmetry can be represented by a linear transformation operator. This operator maps the position vectors of each point in the structure to its corresponding reflected point. In addition, the mode shapes are eigenvectors of this operator [35]. The reflection-symmetry operator has two eigenvalues, $\lambda = \pm 1$, and the bound-mode shapes are thus even ($\lambda = 1$) or odd ($\lambda = -1$) in the compact region about the symmetry axis. We now analyze the consequence of reflection symmetry about the *x* axis. An odd mode shape about the *x* axis will induce a moment and thus rotation about the *x* axis at cross sections *A* and *B* as the side arms move in opposite directions. The sections to the left of cross section *A* and the right of cross section *B* will thus not be at rest and a bound mode is thus not possible with an odd mode shape about the *x* axis. In summary, the bound mode shapes in the compact region will be either even or odd about the *y* axis and will be even about the *x* axis.

B. Modeling with Euler-Bernoulli beam theory and numerical procedure

We derive the governing equations for free vibrations of the structure based on 1D beam theory and discuss the finite element–based procedure to solve them. Let $u(x, t)$ and $u_p(x, t)$ denote the transverse displacements of the main beam and side beam p, respectively. The action functional for this structure is given by

$$S = \int_0^T \int_0^L \left[\frac{\rho A \dot{u}^2}{2} - \frac{EI\left(u''\right)^2}{2} + \sum_{p=1}^N \left(\frac{m\dot{u}^2}{2} + \frac{I_r \dot{\theta}^2}{2} \right) \delta(x - pl) \right] dxdt$$

$$+ \sum_{p=1}^4 \frac{1}{\cos \varphi_p} \int_0^T \int_0^{L_p} \left[\frac{\rho A \dot{u}_p^2}{2} - \frac{\cos^4 \varphi_p EI\left(u_p''\right)^2}{2} + \left(\frac{m_p \dot{u}_p^2}{2} + \frac{\cos^2 \varphi_p I_{rp} \dot{\theta}_p^2}{2} \right) \delta(x - L_p) \right] dxdt, \quad (2)$$

where u' and $\dot{u}$ denote partial derivatives of u with respect to x and t, respectively, $\theta = u'$ is the rotation of the section, $L_p / \cos \varphi_p$ is the length of side beam p, and E, I, ρ, and A are the Young's modulus, bending moment of inertia, density, and cross-section area, respectively. The attached cylinders are assumed to be rigid with diameter d. The bending moment of inertia $I = wt^3/12$ for a beam with width w and thickness t. φ_p is the angle of side beam p with respect to the x axis. We seek harmonic solutions at frequency ω and impose a displacement field of the form $u(x, t) = u(x)e^{i\omega t}$ to replace the time derivatives by $i\omega$. The displacement field satisfies the Euler-Lagrange equations, obtained by our setting variation of S to zero. This condition gives

$$\delta S = \int_0^L \left[-\omega^2 \left(\rho A u \delta u + \sum_{p=1}^N (m u \delta u + I_r u' \delta u') \delta(x - pl) \right) - EI u'' \delta u'' \right] dx$$

$$+ \sum_{p=1}^4 \frac{1}{\cos \varphi_p} \int_0^{L_p} \left[-\omega^2 \left(\rho A u_p \delta u_p + \left(m_p u_p \delta u_p + \cos^2 \varphi_p I_{rp} u_p' \delta u_p' \right) \delta(x - L_p) \right) - \cos^4 \varphi_p EI u_p'' \delta u_p'' \right] dx = 0. \quad (3)$$

We now discuss the numerical procedure to discretize and solve Eq. (3). We use a finite-element approximation, where the unknown degrees of freedom are restricted to be the displacements u and rotations u' at the locations of attached masses. We express u and u' at a point in the structure as a weighted sum of piecewise cubic polynomials, i.e., having continuous first derivatives, and the weights being the degrees of freedom. We seek a solution that satisfies the governing equation (3) for any perturbation fields δu and $\delta u'$ that lie in the same space spanned by the degrees of freedom. Explicit expressions for the polynomials and the resulting equations are presented in Appendix A. The resulting discretized eigenvalue problem for the structure may be written in matrix form as

$$\omega^2 \boldsymbol{M} \boldsymbol{u} = \boldsymbol{K} \boldsymbol{u}, \quad (4)$$

where $\boldsymbol{u}$ is the vector of unknown degrees of freedom, i.e., displacements and rotations at masses, and $\boldsymbol{M}$ and $\boldsymbol{K}$ are the discretized mass and stiffness matrices, respectively.

III. NUMERICAL SOLUTION OF ARCHITECTED BEAMS SUPPORTING BICS

In this section, the mode shapes of BICs and a family of side beams that support these BICs are determined for a given main beam. Although our studies are presented for a specific choice of compact region, the concept and approach can be extended to an arbitrary-sized compact region and material properties. A two-step process is used to design BIC-supporting structures with use of the beam model introduced in Sec. II B. The first step is to determine the bound mode frequencies by imposing zero displacement and rotation at cross sections A and B in the main beam. The next step is to determine the side-beam dimensions that satisfy the equilibrium conditions required to keep cross sections A and B at rest. Finally, we verify if

these modes are indeed BICs, i.e., if their frequency lies in a passband. We do this by performing a dispersion analysis that yields the passband and stopband frequencies.

A. Bound-mode frequencies and design of side beams

Having derived the governing equations for the proposed structure, we now solve them numerically to determine BICs. The first step is to determine the bound modes by considering the compact region of the main beam only and explicitly enforcing zero displacement and rotation at cross sections A and B in Fig. 1(a). The resulting modes will, in general, not satisfy equilibrium conditions at cross sections A and B. The second step is to determine the side-beam dimensions so that the total structure (main and side beams together) satisfies the equilibrium conditions at cross sections A and B. In these mode shapes, cross sections A and B will thus be at rest and have zero net force and moment, thereby ensuring that parts outside the compact region will be at rest. Thus, this procedure ensures there are bound modes in the structure.

In the first step, to determine the natural frequency and mode shape of BICs, we use the material properties of aluminum 6061 (Young's modulus $E = 68.9$ GPa, Poisson's ratio $\nu = 0.3$, and density $\rho = 2700$ kg/m^3) for the beam and neodymium magnet N35 (cylinder density, $\rho_c = 7537.6$ kg/m^3) for the cylinders considering ease of fabrication. The key geometric variables l, w, t, d, and h in the unit cell, see Fig. 1(b), are chosen to be 27.5, 5, 2.032, 5, and 4.6 mm, respectively. The bound mode shapes and frequencies are determined by solving the eigenvalue problem (4) in the compact region with zero-displacement and zero-rotation boundary conditions. Figure 2(a) displays the frequencies of the six bound modes.

Next we need to determine the side-beam dimensions so that the structure supports BICs in the compact region. There are several geometric variables for the side beams as shown in Fig. 1(b) for a unit cell as well as the angle between the main beam and side beam AC, φ_1, as shown in Fig. 1(a). Different sets of geometric variables for the side beams can give BICs in the compact region. We fix φ_1 as 45° to simplify the problem. Also, for ease of fabrication, the beam thickness and the cylinder diameters in the side beams are chosen to be the same as those in the main beam. Thus, the design reduces to determining three geometric variables: length (l_s), width (w_s) of the side beams, and the cylinder height (h_C) at cross section C in Fig. 1(a).

We summarize the conditions on a side-beam displacement field u_p needed to get a BIC. These conditions ensure that cross section A and the region to the left of it will be at rest. Recall the key idea that the two identical side beams at cross section A, as in Fig. 1(a), move out of phase with the main beam, thereby canceling the force and moment at cross section A. Its displacement field has to satisfy the governing equation (3) at bound-mode frequency ω under fixed boundary conditions at cross section A ($u_p = 0$
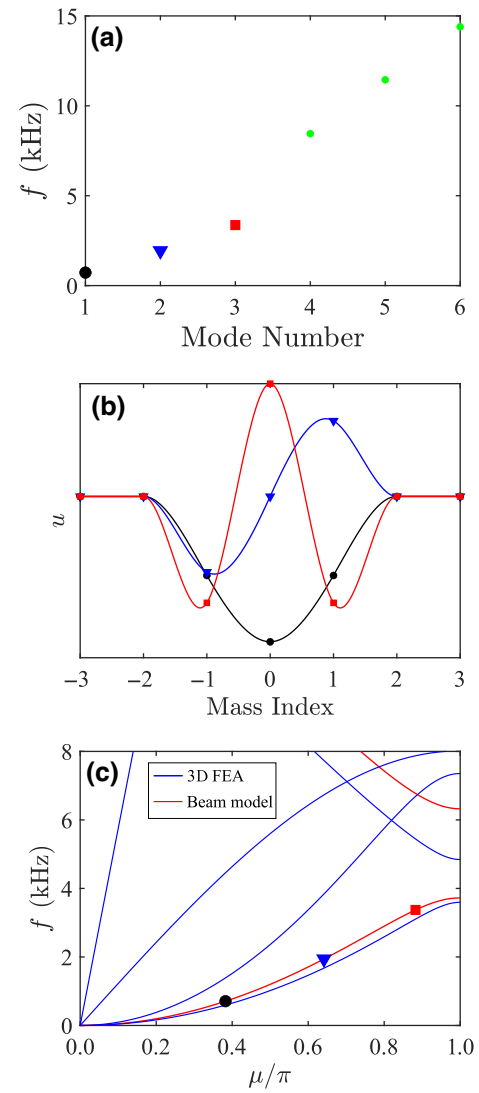
FIG. 2. (a) Frequencies of bound modes in the compact region in Fig. 1(a). (b) Mode shapes of the first three modes. u is the transverse displacement along the main beam. Markers indicate rigid mass locations, with markers the same as those in (a) for the frequency. (c) Dispersion diagram for the main beam from 1D beam theory and 3D elasticity. The frequencies of the first-three modes lie on the lowest flexural band and these modes are thus BICs.

and $u'_p = 0$). In addition, the resulting forces and moments from the side and main beams should add to zero so that cross section A is in equilibrium. Under the 1D beam theory considered, the force and moment at cross section A are given by

$$F = EIu''' + \sum_{p=1}^{2} \cos^3 \varphi_p EI_p u_p''',$$

$$M = EIu'' + \sum_{p=1}^{2} \cos^2 \varphi_p \, EI_p u_p''.$$

We now derive the discrete approximations of the above-mentioned conditions for the side beam having cross section C in Fig. 1(a). We model a side beam using a single finite element and the degrees of freedom are the displacements and rotations at the two ends (cross sections A and C). Since we seek solutions with cross section A fixed, the displacement field simplifies to $u_p(x) = N_3(x/l_s)\theta_C + N_4(x/l_s)u_C$. Explicit expressions for N_3 and N_4 are presented in Appendix A. Under this approximation, the governing equations of side beams and the equilibrium conditions at cross section A then reduce to

$$\delta\theta_C = 0 \implies \left(\frac{4EI_s}{l_s} - \frac{\omega^2 m_s}{420}(4l_s^2 + I_C)\right)\theta_C$$
$$+ \left(\frac{11\omega^2 m_s}{210}l_s - \frac{6EI_s}{l_s^2}\right)u_C = 0, \quad (5a)$$

$$\delta u_C = 0 \implies \left(\frac{11\omega^2 m_s}{210}l_s - \frac{6EI_s}{l_s^2}\right)\theta_C$$
$$+ \left(\frac{12EI}{l_s^3} - \frac{\omega^2 m_s}{420}(156 + m_C)\right)u_C = 0, \quad (5b)$$

$$F_A = 0 \implies \frac{4EI_s}{l_s}\theta_C - \frac{12EI_s}{l_s^2}u_C$$
$$- \frac{2EI}{l_e}\theta_G + \frac{6EI}{l_e^2}u_G = 0, \quad (5c)$$

$$M_A = 0 \implies \frac{12EI_s}{l_s^2}\theta_C - \frac{24EI_s}{l_s^3}u_C$$
$$- \frac{6EI}{l_e^2}\theta_G + \frac{12EI}{l_e^3}u_G = 0, \quad (5d)$$

where $m_s = \rho l_s w_s t$ and $I_s = w_s t^3/12$ are the mass and bending moment of inertia of the side beam, respectively, $m_C = \pi\rho_c d^2 h_C/4$ and $I_C = m_C/12(3d^2/4 + h_C^2)$ are the mass and mass moment of inertia of the cylindrical mass at cross section C, and u_G and θ_G are the displacement and rotation at cross section G, corresponding to the mode shape of the compact region at frequency ω [see Figs. 2(a) and 2(b)]. The force and moment balance constraints assume that the two side beams at cross section A move in phase. Indeed, as discussed earlier, a BIC mode shape is symmetric about the x axis.

The conditions for getting a BIC lead to a system of four nonlinear equations [Eqs. (5a)–(5b)] with five unknown
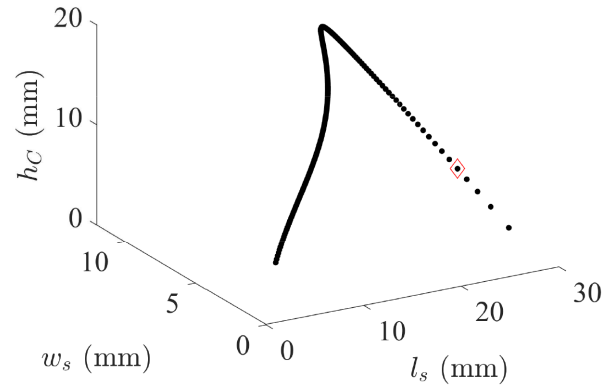
FIG. 3. A one-parameter family of side beams support the lowest-frequency BIC [black marker in Fig. 2(b)]. The geometric dimensions marked with a diamond are used for the experimental demonstration in Sec. IV.

variables (u_C, θ_C, l_s, w_s, and h_C) related to the side beams. To determine them, l_s is set to different fixed values in a wide range and the remaining variables are determined with the Newton-Raphson method. We determined side-beam dimensions that support the lowest-frequency bound mode at 713 Hz, denoted by a black marker in Fig. 2(a). Figure 3 displays a one-parameter family of solutions that we obtained as l_s is varied. Side beams for every solution in Fig. 3 induce the bound mode shown by the black curve in Fig. 2(b). For the chosen main beam, we are unable to find any valid solutions for side beams with rigid masses removed (corresponding to rigid cylinder height $h_C = 0$). Also, design parameters that support BICs at frequencies marked by blue triangle and red square are displayed in Fig. 10 in Appendix E.

B. Dispersion analysis of the architected beams

To confirm if the bound modes in Fig. 2(b) are indeed BICs, i.e., if their frequency lies in the passband, we perform a dispersion analysis of the main beam, which is periodic with the unit cell in Fig. 1(b). We work with the discrete approximation, where the degrees of freedom are u_n and θ_n at a section having rigid mass labeled "n." We seek traveling-wave solutions of the form $\boldsymbol{u}_n = \tilde{\boldsymbol{u}}e^{i\kappa n}$, where κ is the nondimensional wave number, $\boldsymbol{u}_n = [\theta_n, u_n]^T$, and $\tilde{\boldsymbol{u}} = [\theta\ u]^T$. The discretized governing equation (4) for this section then reduces to an eigenvalue problem $\omega^2 \boldsymbol{M}_n(\kappa)\tilde{\boldsymbol{u}} = \boldsymbol{K}_n(\kappa)\tilde{\boldsymbol{u}}$ with

$$\boldsymbol{M}_n(\kappa) = \frac{m_b}{420}\begin{bmatrix} 2l_e^2(4 - 3\cos\kappa) + I_{y_n} & 26l_e\sin\kappa \\ -26il_e\sin\kappa & 312 + 108\cos\kappa + m_n \end{bmatrix}, \quad (6a)$$

$$\boldsymbol{K}_n(\kappa) = \frac{EI}{l_e^2}\begin{bmatrix} 4l_e(2 + \cos\kappa) & -12i\sin\kappa \\ 12i\sin\kappa & 24/l_e(1 - \cos\kappa) \end{bmatrix}. \quad (6b)$$

Solving the eigenvalue problem for each κ in the interval from 0 to π gives two dispersion branches denoted by red curves in Fig. 2(c). The frequencies of the first-three bound modes in Fig. 2(a) lie on the lower red branch, implying that these are BICs.

IV. THREE-DIMENSIONAL NUMERICAL SIMULATIONS AND EXPERIMENTAL RESULTS

In this section we present the verification of our predictions based on the 1D beam model using 3D elasticity theory. The simulations are performed with COMSOL MULTIPHYSICS. Finally, we report on the experimental observation of a BIC under dynamic excitation with a shaker.

A. Verification using 3D elasticity theory

We model the finite beam structure shown in Fig. 4(b) using 3D elasticity theory. Here the motion at every point in a structure made of a linear elastic isotropic solid is governed by [36] $\rho\ddot{\boldsymbol{u}} - [(\lambda + \mu)\nabla(\nabla\cdot\boldsymbol{u}) + \mu\nabla^2\boldsymbol{u}] = 0$, with $\boldsymbol{u} = [u_x \ u_y \ u_z]^T$ being the vector of displacement components, and μ and λ being the Lamé constants of the solid. A finite-element analysis is performed with COMSOL MULTIPHYSICS and the domain is discretized with use of quadratic elements with tetrahedral geometry.

We first verify if the 1D beam model is accurate by comparing the corresponding dispersion surfaces for the unit cell in Fig. 1(b). Figure 2(c) displays this comparison, with the blue and red curves determined with the 3D and 1D models, respectively. The lower-frequency flexural branch is quite close for the two models, which demonstrates the effectiveness of the 1D beam model in predicting flexural mode–based BICs. In addition, the 3D analysis also shows a quadratic bending branch along the y direction and linear longitudinal and torsional dispersion branches.

We now determine the final design using 3D finite-element analysis. All cylinders attached to the main

and side beams are taken to be identical to simplify fabrication. Our starting design point is indicated by the diamond marker in Fig. 3, with side-beam dimensions $l_s = 28$ mm, $w_s = 5.81$ mm, and $h_C = 5.37$ mm. We perform a detailed 3D analysis and make minor changes to the design predicted with use of the 1D beam theory. There are two reasons for requiring modifications to the design predicted with use of the 1D model. First, the rigid masses are assumed to be point masses and the space occupied due to the finite diameter d is ignored in the 1D model. The second reason is to simplify assembly of masses in the side beams; the side beam is made longer, to 40 mm, and masses are attached at distance l_s, as shown in Fig. 4(b). This design is distinct from the 1D beam model, where the cylindrical masses on the side beams are attached at their ends.

We search for suitable l_s and w_s by doing a parametric sweep over these variables near the starting design point using 3D finite-element simulations. This choice is guided by the existence of a one-parameter family of valid design solutions of Eq. (5); see Fig. 3. The sweep search yields $l_s = 28$ mm and $w_s = 8.23$ mm when the height and diameter of all the attached cylinders are set to 4.6 and 5 mm, respectively. Figure 5(a) displays the BIC mode shape confined to the compact region for these side-beam dimensions. Note that the frequency determined with the 3D model (682.5 Hz) is close to that predicted with the 1D model (713 Hz). To verify that the mode is indeed a BIC, we examine the energies of sections inside and outside the compact region in Appendix B. Our bound modes lie in the category of Fabry-Perot BICs, where a wave is confined between reflection symmetric resonators [25,26]. We analyze the mode shape and frequency of a design that violates reflecting symmetry about the y-axis in Appendix D.

B. Experimental observation of a BIC

Finally, we report on the experimental observation of the BIC shown in Fig. 5(a) using the dimensions determined
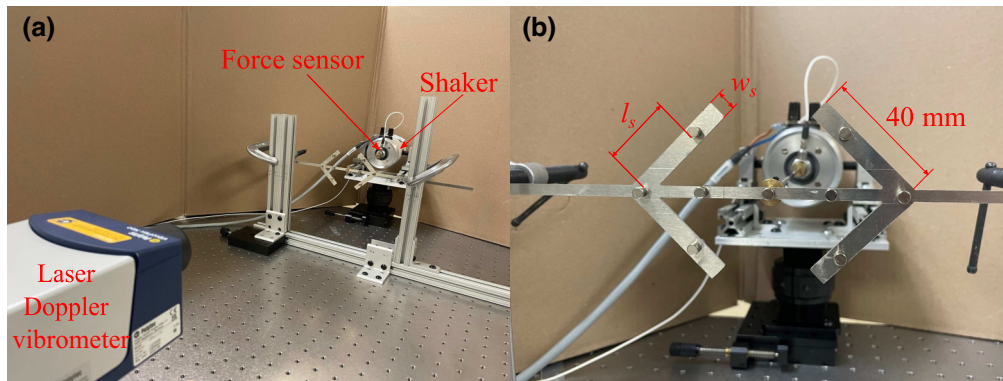
FIG. 4. (a) Experimental setup. The beam is excited at the center of the compact region with use of a shaker. A force sensor is attached to the shaker. The velocity at various points along the beam is measured with a laser vibrometer. (b) Enlarged view, indicating the dimensions l_s and w_s in a side beam of length 40 mm.
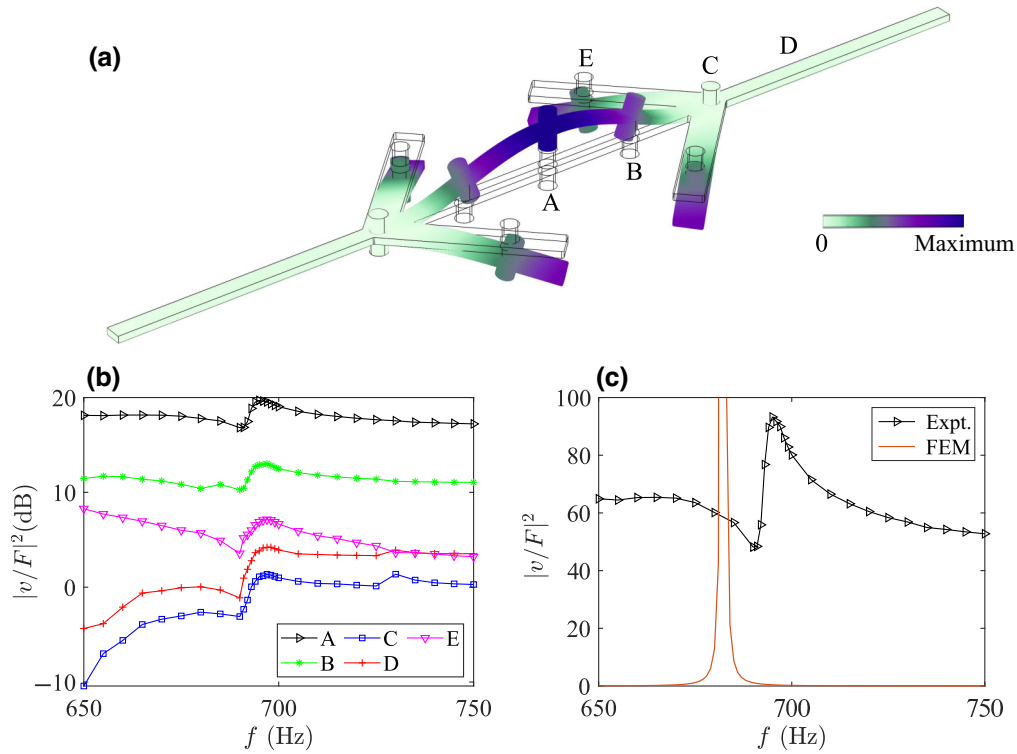
FIG. 5. (a) BIC mode shape at 682.5 Hz determined by 3D finite-element analysis. (b) Measured frequency response at cylinders. A resonant peak occurs at 695 Hz, corresponding to the BIC. (c) Comparison of frequency response at excitation point A: lossless simulation and experiments. FEM, finite-element method.

from the 3D analysis. The experimental setup is shown in Fig. 4(a). The structure in Fig. 4(b) is fabricated from a 0.08-in.-thick aluminum 6061 sheet by water-jet cutting. Cylindrical neodymium magnets N35 of 5-mm diameter and 4.6-mm height are placed at the top and bottom in the main and side beams. These dimensions are chosen since they are commercially available. The sample is clamped at both ends and a permanent-magnet shaker (LDS V203, Brüel & Kjær) is used to apply sinusoidal displacement at the center of the compact region. The excitation point is denoted here by point A, as shown in Fig. 5(a). A force sensor (PCB Piezotronics 208C01) is attached to the shaker to measure the applied force. The velocity at various points along the main beam is measured with a laser Doppler vibrometer (Polytec VFX-I-110).

We summarize the experimental procedure. We excite the structure at different frequencies in the interval from 650 to 750 Hz and determine the frequency response function. The excitation frequencies are indicated by markers in the response plot in Fig. 5(a). The velocity of a cylinder and the force applied by the shaker are measured by applying the excitation at a given frequency for 15 s. To allow transients to die down, the force and velocity data are recorded in the last 6 s of excitation. Then the beam is kept at rest for 10 s before it is excited at the next frequency. This process is repeated to measure the velocity of each cylinder. The maximum velocity, v and maximum force,

F, at a given frequency are calculated by a FFT of the measured velocity and force. Then, the normalized energy of every point is determined as $|v/F|^2$.

Figure 5(b) displays the measured response at cylinders on the right side of the excitation point. We observe a peak in the frequency response of the excitation point A at 695 Hz. At this frequency, the responses at points C and D, lying at the boundary and outside the compact region, are significantly lower (1 unit) compared with response at the excitation point A (about 93 units). This observation confirms the existence of a BIC in the structure at 695 Hz. We also measured the frequency response at other cylinders left of the excitation point. Note that due to reflection symmetry, the corresponding symmetric points on the left should have identical response. We quantified the difference in response at points B, C, and D and the side beams with their corresponding symmetric points to the left at the BIC frequency. Our experiments showed a 3% difference at point B and at the side beams, and a 10% difference at points C and D with their corresponding symmetric points to the left.

Figure 5(c) displays a comparison between experiments and lossless simulations for the frequency response at the excitation point. The simulation has a response peak (around 1000 units) at 682.5 Hz, which is the frequency of the mode shape in Fig. 5(a). We remark on the various sources of error that result in deviation from a true

BIC. We conducted additional simulations to identify the source of discrepancy between simulations and experiments. In particular, we conducted simulations considering material loss and perturbed geometry. Details are presented in Appendix C. The discrepancy between experiments and simulations is attributed to imperfections in manufacturing, with the fabricated beam width being around 4.8 mm instead of the designed 5 mm, and precision in placing cylinders at the exact locations. Since our numerical simulation with 3D finite-element analysis predicts high quality factors, we believe the mismatch between simulation and experiments arises from limitations of our fabrication and assembly process. However, this is not a fundamental limitation of the proposed framework and it is one that can be addressed in principle. Indeed, with recent advances in precision machining at the microscale and the nanoscale, we believe that the quality factor can approach that predicted by numerical simulations.

Finally, we note that the frequency response at point C is 0.137 units in simulations, compared with 1000 for point A. Although this is significantly lower than the experimental value, it is not zero, in contrast to the prediction of the 1D beam model. To understand this discrepancy, note that the Euler-Bernoulli beam theory, which is used to predict a true BIC, assumes that each cross section is nondeformable, and undergoes translations and rigid rotations [37]. Although this beam theory is an excellent approximation at low frequencies, small deviations arise when full 3D effects are considered. The resulting displacement at point C is thus a measure of the deviation of the exact 3D solution from the 1D beam theory. Notably, we do not attempt to satisfy the zero-displacement condition pointwise, but instead we do it in an average sense over the entire cross section.

V. CONCLUSION

We introduce an architected structure that comprises a main beam with periodically attached masses and has a compact region with protruding side beams. Symmetry and equilibrium constraints are used to determine the conditions required for a BIC in this compact region. A 1D beam model is derived with use of Euler-Bernoulli theory, and a finite-element method is used to determine bound modes in the structure. The conditions on main and side beams required to support a BIC are derived, and a Newton-Raphson method is used to solve the resulting nonlinear equations. For each BIC, we find a one-parameter family of side-beam designs that supports it. A dispersion analysis is conducted to confirm that their frequencies lie in the passband and they are thus BICs.

We verify the predictions of BICs based on the 1D beam model using finite-element analysis based on 3D elasticity. The 1D model is found to be in good agreement for the low-frequency flexural modes under consideration.

For ease of fabrication and assembly, and to account for the mismatch with 3D elasticity, minor modifications to the side-beam design determined with the 1D model are made by doing a parametric sweep over the width and length of side beams using 3D finite-element analysis. The designed structure is fabricated and excited over a range of frequencies around the BIC frequency. The experimental results for frequency response at the excitation point show a resonant peak close to the frequency predicted by finite-element analysis. At the resonant frequency, the fraction of energy leaking to the surroundings is reduced to a minimum, which demonstrates the existence of a BIC in the compact region. The experimental results are compared with results from finite-element analysis, and the possible reasons for discrepancies, along with causes of deviation from a true BIC, are discussed.

We remark on some future possible extensions of our work. These concepts translate across length scales and material properties, and may find applications at the microscale and the nanoscale. At those scales, the limitations associated with material damping may be significantly reduced. The idea of canceling forces and moments by exploiting symmetry may be extended to realize bound modes and BICs in plates, shells, and 3D architected solids. Our framework is relevant in physical domains beyond the elastic structures considered here—for instance, in photonic crystal waveguides with off-channel defects, in which BICs were predicted earlier [26].

APPENDIX A: FINITE-ELEMENT SHAPE FUNCTIONS AND MATRICES

We discuss an approximation we use to determine the effective bending stiffness of the beam segment between cross sections 1 and 2 in Fig. 6. Its contribution comes from three segments: the two segments of length $d/2$ at the two ends having rigid masses, and the beam segment with length $l_e = l - d$ between them. These three segments may be viewed as springs in series, and their effective stiffness is lower than the stiffness of these segments. The segment having rigid masses (length $d/2$) has significantly greater bending stiffness and its contribution to the effective bending stiffness is ignored. Only the beam segment with length l_e in Fig. 6 is used to determine the effective bending stiffness. Under this approximation, the rigid masses may be represented as point masses with a beam segment of length l_e between them.

Figure 6 displays a schematic of a beam finite element. The discrete degrees of freedom are the displacements and rotations at the location of rigid masses, labeled $[\theta_1,\ u_1]^T$
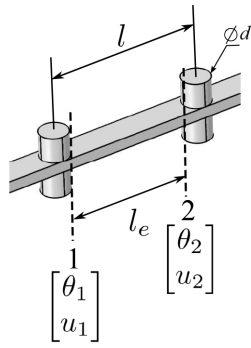
FIG. 6. A beam finite element with degrees of freedom $[\theta_1, u_1]^T$ and $[\theta_2, u_2]^T$ at cross sections 1 and 2, respectively.

and $[\theta_2, u_2]^T$ in Fig. 6. We denote the locations of cross sections 1 and 2 by x_1 and x_2, respectively. In this element, we seek a solution of the form

$$u(x) = N_1(\xi)\theta_1 + N_2(\xi)u_1 + N_3(\xi)\theta_2 + N_4(\xi)u_2, \quad \text{(A1)}$$

where ξ is a local coordinate in the element given by $(x - x_1)/l_e$ and taking values in $[0, 1]$, $N_i(\xi)$ are Hermite polynomial shape functions [38], and

$$N_1 = l_e\xi(\xi - 1)^2, \quad \text{(A2a)}$$

$$N_2 = 1 - 3\xi^2 + 2\xi^3, \quad \text{(A2b)}$$

$$N_3 = l_e\xi^2(\xi - 1), \quad \text{(A2c)}$$

$$N_4 = \xi^2(3 - 2\xi) \quad \text{(A2d)}$$

are explicit expressions for the shape functions. Equation (A1) may be written compactly as $u(x) = N u^T$, with N and u being vectors having components N_i and u_i, respectively.

We derive the contribution of the beam segment described above to the governing equation. We substitute Eq. (A1) into Eq. (3) and separate the terms with and without ω^2 into the mass matrix, M_{el}, and the stiffness matrix, K_{el}, respectively, for an element. The various terms in Eq. (3) then have the form $\delta u^T K_{\text{el}} u$ or $\omega^2 \delta u^T M_{\text{el}} u$, where

$$K_{\text{el}} = \int_{x_1}^{x_2} \frac{d^2 N^T}{dx^2} EI \frac{d^2 N}{dx^2} dx, \quad \text{(A3)}$$

$$M_{\text{el}} = \int_{x_1}^{x_2} \rho A N^T N \, dx$$
$$+ \sum_{i=1}^{2} m_i N^T(\xi_i) N(\xi_i) + \sum_{i=1}^{2} I_i \frac{dN^T(\xi_i)}{dx} \frac{dN(\xi_i)}{dx}, \quad \text{(A4)}$$

where x_1 and x_2 are, respectively, the locations of cross sections 1 and 2 in Fig. 6, and m_i and I_i represent the mass and

mass moment of inertia of the ith rigid mass, respectively. Explicit expressions for these matrices are given as

$$M_{\text{el}} = \frac{m_b}{420} \begin{bmatrix} 4l_e^2 + I_1 & 22l_e & -3l_e^2 & 13l_e \\ 22l_e & 156 + m_1 & -13l_e & 54 \\ -3l_e^2 & -13l_e & 4l_e^2 + I_2 & -22l_e \\ 13l_e & 54 & -22l_e & 156 + m_2 \end{bmatrix}, \quad \text{(A5a)}$$

$$K_{\text{el}} = \frac{EI}{l_e^3} \begin{bmatrix} 4l_e^2 & 6l_e & 2l_e^2 & -6l_e \\ 6l_e & 12 & 6l_e & -12 \\ 2l_e^2 & 6l_e & 4l_e^2 & -6l_e \\ -6l_e & -12 & -6l_e & 12 \end{bmatrix}, \quad \text{(A5b)}$$

where $m_b = \rho A l_e$ is the mass of the beam in the element. Assembling M_{el} and K_{el} for every beam segment in the structure gives its mass matrix M and stiffness matrix K. The governing equations result in an eigenvalue problem $\omega^2 M u = K u$, where u is a vector with components having the displacements and rotations at the rigid mass locations.

APPENDIX B: TRANSMITTANCE TO THE FAR FIELD

To verify that the mode in Fig. 5(a) is indeed a BIC, the conventional approach is to determine the transmittance into the far field near the BIC frequencies [39]. Since we are working with a finite structure, we instead determine the ratio of kinetic energies at cross sections inside and outside the compact region (cross sections A and D in Fig. 5(a)) at the steady state. This computation is done by 3D finite-element analysis. Figure 7 shows that the ratio $(v_D/v_A)^2$ goes to zero at the mode's frequency, thus verifying its BIC property.
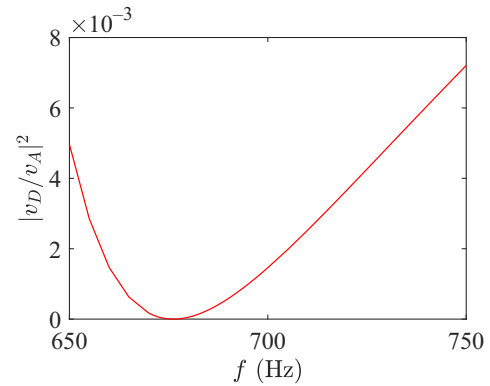
FIG. 7. Ratio of kinetic energies at points outside and inside the compact region goes to zero at the BIC frequency. Steady-state results from 3D finite-element analysis.

APPENDIX C: SIMULATIONS WITH MATERIAL LOSS AND IMPERFECT GEOMETRY

To identify the source of discrepancy between simulations and experiments, we conducted simulations for two other cases that consider material loss and deviation from the exact geometry:

(a) Considering material loss. We consider a loss factor of 0.01 for both aluminum and the magnet.

(b) Introducing perturbation in the 3D model. We change the location of every cylinder pair from the location in the theoretical design by a random value in the interval from −4% to 4% of the unit-cell length along the corresponding beam axis. This perturbation aims to consider the error caused by attaching the magnets by hand in the structure.

The frequency response for all cases, including the simulation with lossless perfect geometry, is presented in Fig. 8. Also shown is the experimentally measured response. We observe that the effect of material loss (blue curve) is negligible on the quality factor. In contrast, the change in geometry due to deviation in the magnet location (red curve) results in a significant reduction in the quality factor, as well as a shift in frequency. A similar frequency shift is also observed in the experiment. On the basis of these results, we conclude that imperfections in manufacturing and assembly have a more significant effect on the quality factor than material loss in the frequency regimes considered.
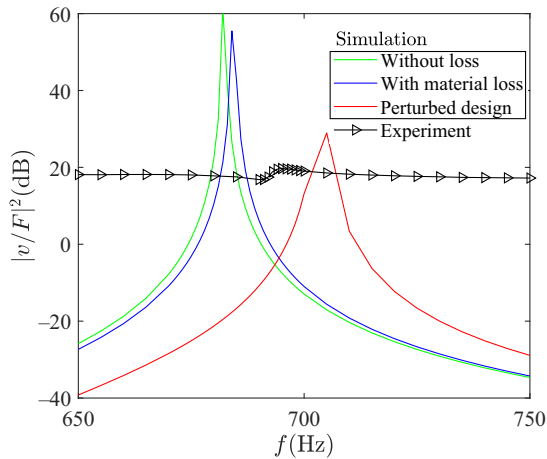
FIG. 8. Frequency response at the excitation point obtained with 3D FEA for three cases: (a) no loss and perfect geometry (green curve); (b) with material loss (blue curve); and (c) modified magnet location in side arms (red curve). Experimental response also shown (black curve). Perturbing the geometry has a more significant effect on quality factor compared with material loss.

APPENDIX D: EFFECT OF BREAKING SYMMETRY ABOUT THE y AXIS

We demonstrate the effect of violating reflection symmetry in the proposed design. To this end, we performed 3D finite-element analysis on a design that breaks reflection symmetry about the y axis, as shown in Fig. 9(a). We change the rigid-cylinder locations on the right side beams. The mode shape localized in the compact region now has a frequency (756 Hz) different from the BIC frequency (682.5 Hz). The out-of-plane displacement of this mode is illustrated in Fig. 9(b). We observe that the region to the left of the compact region experiences a lower leakage than the region on the right side.

We remark that a BIC can, in principle, be supported on asymmetric side beams, in which case, the left and right side beams will have to be designed separately. In particular, they need to satisfy the constrains for force and moment equilibrium and conditions of zero degrees of freedom, as discussed in Sec. III.

APPENDIX E: ONE-PARAMETER FAMILY OF DESIGNS FOR OTHER BICS

We find families of design parameters for the BICs at frequencies marked by blue triangle and red square in Fig. 2(a) following the same procedure discussed in Section III A.

Similarly for the frequencies marked by a blue triangle and a red square, we find families of design parameters that support the corresponding bound modes in Fig. 2(b).
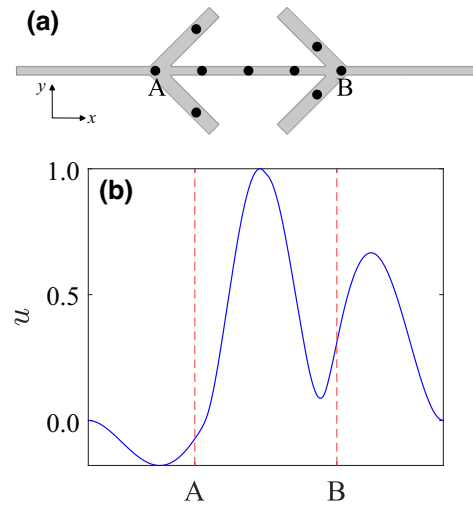
FIG. 9. (a) A structure violating reflection symmetry about the y axis. Attached cylinders are marked by black circles. (b) Out-of-plane displacement along the main beam at 756 Hz, which is the closest to the observed BIC frequency. The BIC in the compact region between cross sections A and B cannot exist due to violation of symmetry about the y axis.
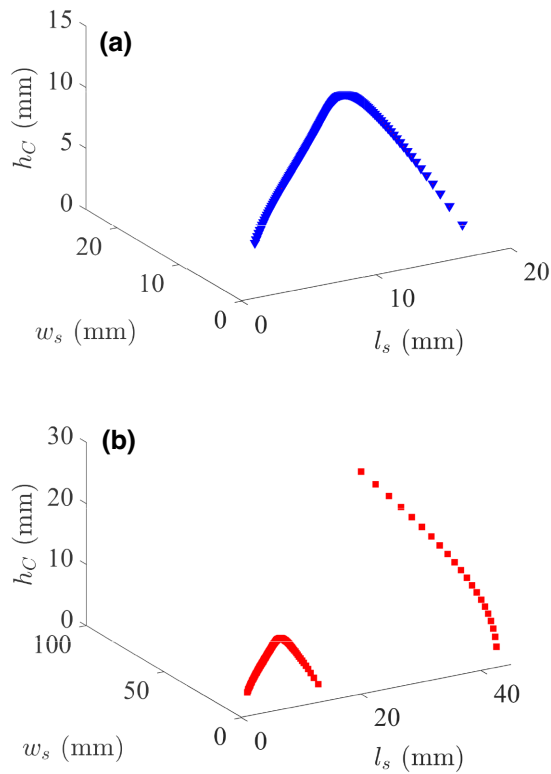
FIG. 10. One-parameter family of side-beam design that support the BICs marked by (a) blue and (b) red markers in Fig. 2(b). The curve in (b) is continuous. It looks discontinuous as the design variables take negative values (not shown).

[1] C. W. Hsu, B. Zhen, A. D. Stone, J. D. Joannopoulos, and M. Soljačić, Bound states in the continuum, Nat. Rev. Mater. **1**, 1 (2016).

[2] S.-H. Jo, H. Yoon, Y. C. Shin, and B. D. Youn, A graded phononic crystal with decoupled double defects for broadband energy localization, Int. J. Mech. Sci. **183**, 105833 (2020).

[3] A. Khelif, A. Choujaa, B. Djafari-Rouhani, M. Wilm, S. Ballandras, and V. Laude, Trapping and guiding of acoustic waves by defect modes in a full-band-gap ultrasonic crystal, Phys. Rev. B **68**, 214301 (2003).

[4] R. Marchal, O. Boyko, B. Bonello, J. Zhao, L. Belliard, M. Oudich, Y. Pennec, and B. Djafari-Rouhani, Dynamics of confined cavity modes in a phononic crystal slab investigated by in situ time-resolved experiments, Phys. Rev. B **86**, 224302 (2012).

[5] J. von Neumann and E. P. Wigner, Über merkwürdige diskrete Eigenwerte, in *Phys.Z.*, Vol. 30 (1929), p. 465.

[6] L. Fonda, Bound states embedded in the continuum and the formal theory of scattering, Ann. Phys. (N. Y) **22**, 123 (1963).

[7] F. H. Stillinger and D. R. Herrick, Bound states in the continuum, Phys. Rev. A **11**, 446 (1975).

[8] R. Parker, Resonance effects in wake shedding from parallel plates: Some experimental observations, J. Sound. Vib. **4,** 62 (1966).

[9] K. Koshelev, A. Bogdanov, and Y. Kivshar, Meta-optics and bound states in the continuum, Science Bulletin **64**, 836 (2019).

[10] M. Imada, S. Noda, A. Chutinan, T. Tokuda, M. Murata, and G. Sasaki, Coherent two-dimensional lasing action in surface-emitting laser with triangular-lattice photonic crystal structure, Appl. Phys. Lett. **75**, 316 (1999).

[11] K. Hirose, Y. Liang, Y. Kurosaka, A. Watanabe, T. Sugiyama, and S. Noda, Watt-class high-power, high-beam-quality photonic-crystal lasers, Nat. Photonics **8**, 406 (2014).

[12] A. Kodigala, T. Lepetit, Q. Gu, B. Bahari, Y. Fainman, and B. Kanté, Lasing action from photonic bound states in continuum, Nature **541**, 196 (2017).

[13] S. Romano, G. Zito, S. N. L. Yépez, S. Cabrini, E. Penzo, G. Coppola, I. Rendina, and V. Mocellaark, Tuning the exponential sensitivity of a bound-state-in-continuum optical sensor, Opt. Express **27**, 18776 (2019).

[14] L. L. Doskolovich, E. A. Bezus, and D. A. Bykov, Integrated flat-top reflection filters operating near bound states in the continuum, Photon. Res. **7**, 1314 (2019).

[15] J. M. Foley, S. M. Young, and J. D. Phillips, Symmetry-protected mode coupling near normal incidence for narrow-band transmission filtering in a dielectric grating, Phys. Rev. B **89**, 165111 (2014).

[16] O. Kawachi, S. Mineyoshi, G. Endoh, M. Ueda, O. Ikata, E. Hashimoto, and M. Yamaguchi, Optimal cut for leaky saw on LiTaO/sub 3/for high performance resonators and filters, IEEE Trans. Ultrason. Ferroelectr. Freq. Control **48**, 1442 (2001).

[17] N. F. Naumenko and B. P. Abbott, Surface acoustic wave devices using optimized cuts of a piezoelectric substrate (2003), US Patent 6,556,104.

[18] L. Cao, Y. Zhu, S. Wan, Y. Zeng, Y. Li, and B. Assouar, Perfect absorption of flexural waves induced by bound state in the continuum, Extreme Mech. Lett. **47**, 101364 (2021).

[19] F. Benabid, J. C. Knight, G. Antonopoulos, and P. S. J. Russell, Stimulated Raman scattering in hydrogen-filled hollow-core photonic crystal fiber, Science **298**, 399 (2002).

[20] F. Couny, F. Benabid, P. Roberts, P. Light, and M. Raymer, Generation and photonic guidance of multi-octave optical-frequency combs, Science **318**, 1118 (2007).

[21] A. Rahman and R. K. Pal, Bound modes in the continuum based phononic waveguides, J. Appl. Phys. **132**, 115109 (2022).

[22] C. W. Hsu, B. Zhen, J. Lee, S.-L. Chua, S. G. Johnson, J. D. Joannopoulos, and M. Soljačić, Observation of trapped light within the radiation continuum, Nature **499**, 188 (2013).

[23] Z. Sadrieva, M. Belyakov, M. Balezin, P. Kapitanova, E. Nenasheva, A. Sadreev, and A. Bogdanov, Experimental observation of a symmetry-protected bound state in the continuum in a chain of dielectric disks, Phys. Rev. A **99**, 053804 (2019).

[24] Y. Plotnik, O. Peleg, F. Dreisow, M. Heinrich, S. Nolte, A. Szameit, and M. Segev, Experimental observation of optical bound states in the continuum, Phys. Rev. Lett. **107,** 183901 (2011).

[25] D. C. Marinica, A. G. Borisov, and S. V. Shabanov, Bound states in the continuum in photonics, Phys. Rev. Lett. **100,** 183902 (2008).

[26] E. N. Bulgakov and A. F. Sadreev, Bound states in the continuum in photonic waveguides inspired by defects, Phys. Rev. B **78,** 075105 (2008).

[27] A. Taghizadeh and I.-S. Chung, Quasi bound states in the continuum with few unit cells of photonic crystal slab, Appl. Phys. Lett. **111,** 031114 (2017).

[28] D. R. Abujetas, Á. Barreda, F. Moreno, A. Litman, J.-M. Geffrin, and J. A. Sánchez-Gil, High-Q transparency band in all-dielectric metasurfaces induced by a quasi bound state in the continuum, Laser Photon. Rev. **15,** 2000263 (2021).

[29] O. Haq and S. Shabanov, Bound states in the continuum in elasticity, Wave Motion **103,** 102718 (2021).

[30] L. Cao, Y. Zhu, Y. Xu, S.-W. Fan, Z. Yang, and B. Assouar, Elastic bound state in the continuum with perfect mode conversion, J. Mech. Phys. Solids **154,** 104502 (2021).

[31] H. Fan, H. Gao, S. An, Z. Gu, Y. Chen, S. Huang, S. Liang, J. Zhu, T. Liu, and Z. Su, Observation of non-Hermiticity-induced topological edge states in the continuum in a trimerized elastic lattice, Phys. Rev. B **106,** L180302 (2022).

[32] Y. Yu, X. Xi, and X. Sun, Observation of mechanical bound states in the continuum in an optomechanical microresonator, Light: Sci. Appl. **11,** 328 (2022).

[33] H. Tong, S. Liu, M. Zhao, and K. Fang, Observation of phonon trapping in the continuum with topological charges, Nat. Commun. **11,** 1 (2020).

[34] D. Lee, J. Park, S. Kim, J. Mun, J. Kim, X. Piao, N. Park, and J. Rho, Elastic bound states in the continuum by acoustoelastic interaction, Extreme Mech. Lett. **61,** 101965 (2023).

[35] M. S. Dresselhaus, G. Dresselhaus, and A. Jorio, *Group Theory: Application to the Physics of Condensed Matter* (Springer Science & Business Media, Berlin, 2007).

[36] J. Achenbach, *Wave Propagation in Elastic Solids* (Elsevier, Amsterdam, 2012).

[37] J. M. Gere and S. Timoshenko, Mechanics of Materials. ed, Boston, MA: PWS (1997).

[38] R. D. Cook, D. S. Malkus, M. E. Plesha, and R. J. Witt, *Concepts and Applications of Finite Element Analysis, 4th Edition* (Wiley, New York, 2001), 4th ed.

[39] A. F. Sadreev, Interference traps waves in an open system: bound states in the continuum, Rep. Prog. Phys. **84,** 055901 (2021).